Noname manuscript No.
(will be inserted by the editor)

IRNSS/NavIC and GPS: A Single and Dual System L5 Analysis

S. Zaminpardaz · P.J.G. Teunissen · N. Nadarajah

the date of receipt and acceptance should be inserted later

Abstract The Indian Regional Navigation Satellite System (IRNSS) has recently (May 2016) become fully-operational. In this contribution, for the fully-operational IRNSS as a standalone system and also in combination with GPS, we provide a first assessment of L5 integer ambiguity resolution and positioning performance. While our empirical analyses are based on the data collected by two JAVAD receivers at Curtin University, Perth, Australia, our formal analyses are carried out for various onshore locations within the IRNSS service area. We study the noise characteristics (carrier-to-noise density, measurement precision, time-correlation), the integer ambiguity resolution performance (success rates and ambiguity dilution of precision (ADOP)), and the positioning performance (ambiguity float and ambiguity fixed). The results show that our empirical outcomes are consistent with their formal counterparts and that the GPS L5-data have a lower noise level than that of IRNSS L5-data, particularly in case of the code data. The underlying model in our assessments varies from standalone IRNSS (L5) to IRNSS+GPS (L5), from unconstrained to height-constrained and from kinematic to static. Significant improvement of ambiguity resolution and positioning performance are achievable upon integrating L5-data of IRNSS with GPS.

S. Zaminpardaz
GNSS Research Centre, Department of Spatial Sciences, Curtin University, Perth, Australia
E-mail: safoora.zaminpardaz@curtin.edu.au

P. J. G. Teunissen
GNSS Research Centre, Department of Spatial Sciences, Curtin University, Perth, Australia; Department of Geoscience and Remote Sensing, Delft University of Technology, Delft, The Netherlands

N. Nadarajah
GNSS Research Centre, Department of Spatial Sciences, Curtin University, Perth, Australia

Keywords: Indian Regional Navigation Satellite System (IRNSS), Navigation with Indian Constellation (NavIC), GPS Block IIF, Integer ambiguity resolution, ADOP.

1 Introduction

The Indian Regional Navigation Satellite System (IRNSS) has recently (May 2016) become fully-operational and provided with the operational name of NavIC (Navigation with Indian Constellation). It has been developed by the Indian Space Research Organization (ISRO) with the objective of offering positioning, navigation and timing (PNT) to the users in its service area. The IRNSS satellites transmit navigation signals, based on Code Division Multiple Access (CDMA), on L5 (1176.45 MHz) with a Binary Phase-Shift Key (BPSK (1)) modulation for standard positioning service (SPS) users, and with a Binary Offset Carrier (BOC (5,2)) modulation for restricted service (RS) users (ISRO, 2014a). The fully-operational IRNSS constellation has recently been realized, consisting of three geostationary orbit (GEO) satellites and four inclined geosynchronous orbit (IGSO) satellites. The orbital period of the IRNSS satellites is one sidereal day (23 hours and 56 minutes), such that the IRNSS satellite ground tracks repeat every solar day (24 hours) four minutes earlier. Table 1 gives information on the full IRNSS constellation.

Among the published studies on the IRNSS, while some are simulation-based (Mozo Garcia et al, 2010; Sarma et al, 2010; Sekar et al, 2012; Rethika et al, 2013; Rao, 2013), the others are based on using real data. Thoelert et al (2014) assesses the clock stability of IRNSS-1A, while the accuracy of a precise model for solar radiation pressure is tested using the IRNSS-1A and 1B observations in (Kumari et al, 2015). Babu et al (2015) compares orbit determination methods for IRNSS-1A, 1B and 1C, and in order to validate the orbit accuracy with modernized ephemeris parameters, Chan-

drasekhar et al (2015) employs the IRNSS-1A, 1B and 1C real data. Montenbruck and Steigenberger (2015) used the observations of the IRNSS-1A and 1B to investigate the quality of the IRNSS navigation messages. Nadarajah et al (2015), after assessing the IRNSS noise characteristics, combines the L5/E5 signals of IRNSS, GPS, Galileo and QZSS for instantaneous attitude determination. The positioning results over India based on the data of I1, I2, I3, and I4 are presented in (Ganeshan et al, 2015). The first IRNSS standalone positioning results over Australia are presented in (Zaminpardaz et al, 2016b), and Odijk et al (2016) presents the first analysis of the differential inter-system biases (DISBs) between L5 signal of IRNSS w.r.t. the L5/E5a signals of GPS, Galileo and QZSS.

Transmitting L5 frequency shared by three other GNSSs (Global Navigation Satellite Systems), i.e. GPS, Galileo and QZSS, makes the IRNSS interoperable with those systems. All the satellites belonging to the latest generation of GPS, called Block IIF, have been sending out the L5 signal since 2010 as part of the GPS modernization (GPS Directorate, 2011). With the launch of the last satellite of Block IIF on February 2016, it now has all its 12 satellites operational. There exists a few number of studies in the literature making use of the GPS L5 real data. An analysis of the GPS L5 stochastic properties through different GNSS observables combinations is provided by (de Bakker et al, 2012). The GPS L5-based precise point positioning (PPP) results are presented in (Tegedor and Øvstedal, 2014). In (Odijk and Teunissen, 2013; Odijk et al, 2016), the DISBs between GPS L5 and the same signal of other systems are characterized, and Nadarajah et al (2015) combines the L5/E5 signals of GPS, IRNSS, Galileo and QZSS for instantaneous attitude determination.

In this contribution, we provide the very first L5 ambiguity resolution results of the fully-operational IRNSS as a standalone system and also in combination with the fully-operational GPS Block IIF together with the corresponding positioning results. This contribution is organized as follows. In section 2, the unconstrained and weighted height-constrained single-frequency GNSS model of the combined IRNSS+GPS and standalone IRNSS is formulated. The noise characteristics of the IRNSS and GPS L5-signal are presented in section 3 through the carrier-to-noise density, the estimated measurement precision and time correlation. A formal analysis of the position dilution of precision (PDOP) corresponding with the standalone IRNSS and IRNSS+GPS is also provided. This analysis includes the identification and explanation of occurring periods of poor receiver-satellite geometries. Section 4 contains the formal and empirical ambiguity resolution performance analyses on an epoch-by-epoch as well as multi-epoch basis. This is done for the unconstrained and height-constrained model, and for single-system IRNSS and dual-system IRNSS+GPS. The corresponding positioning performance is investigated in section 5, both for ambiguity-float and ambiguity-fixed scenarios. Finally, a summary and conclusions are given in section 6.

Table 1 Information on the IRNSS/NavIC satellites (ISRO, 2014b,c,d, 2015, 2016a,b,c).

Satellite	Type	Longitude	Inclination	Launch date
IRNSS-1A (I1)	IGSO	55° E	29.0°	July 2013
IRNSS-1B (I2)	IGSO	55° E	31.0°	April 2014
IRNSS-1C (I3)	GEO	83° E	–	October 2014
IRNSS-1D (I4)	IGSO	111.75° E	30.5°	March 2015
IRNSS-1E (I5)	IGSO	111.75° E	28.1°	January 2016
IRNSS-1F (I6)	GEO	32.5° E	–	March 2016
IRNSS-1G (I7)	GEO	129.5° E	–	April 2016

2 GNSS Model of Observations

In this section, we formulate the single-baseline single-frequency GNSS model for the combined IRNSS and GPS, from which the standalone IRNSS model follows as a special case. In the sequel, we refer to the IRNSS-specific parameters and the GPS-specific parameters using the subscripts $_I$ and $_G$, respectively.

2.1 Unconstrained Model

Suppose that two receivers are simultaneously tracking m_I IRNSS plus m_G GPS satellites on frequency L5 with the wavelength λ. We assume that the two receivers form a short baseline such that the atmospheric delays and orbital errors are common to both of them, thereby becoming eliminated through between-receiver differencing. We further assume that both receivers are of the same manufacturer (receiver make, type and firmware), thus allowing us to assume that the IRNSS-GPS ISBs are zero (Odijk et al, 2012, 2016). Therefore, instead of classical double-differencing per constellation, inter-system double-differencing can be used, resulting in a higher level of redundancy. For such a set-up, the corresponding full-rank single-epoch model of linearized double-differenced (DD) observation equations reads

$$\begin{aligned} E\begin{bmatrix} D_m^T p \\ D_m^T \phi \end{bmatrix} &= \begin{bmatrix} D_m^T G & 0 \\ D_m^T G & \lambda I_{m-1} \end{bmatrix} \begin{bmatrix} b \\ a \end{bmatrix} \\ D\begin{bmatrix} D_m^T p \\ D_m^T \phi \end{bmatrix} &= \begin{bmatrix} D_m^T Q_{pp} D_m & 0 \\ 0 & D_m^T Q_{\phi\phi} D_m \end{bmatrix} \end{aligned} \tag{1}$$

where $E[.]$ and $D[.]$ denote the expectation and dispersion operator, respectively. With $m = m_I + m_G$, the $(m-1)\times m$ matrix $D_m^T = [-e_{m-1},\ I_{m-1}]$ represents the inter-system differencing operator, where e_{m-1} and I_{m-1} are the $(m-1)$-vector of ones and the identity matrix of $(m-1)$ dimension,

respectively. The combined vectors and matrices can be split into system-specific parts as

$$p = [p_I^T, p_G^T]^T,\ \phi = [\phi_I^T, \phi_G^T]^T,\ G = [G_I^T, G_G^T]^T$$
$$Q_{pp} = 2 \times \text{blkdiag}(\sigma_{p_I}^2 W_I^{-1},\ \sigma_{p_G}^2 W_G^{-1})$$
$$Q_{\phi\phi} = 2 \times \text{blkdiag}(\sigma_{\phi_I}^2 W_I^{-1},\ \sigma_{\phi_G}^2 W_G^{-1})$$

With $* = \{I, G\}$, p_* and ϕ_* denote, respectively, the m_*-vectors of between-receiver single-differenced (SD) "observed-minus-computed" code and phase observables. The $m_* \times 3$ matrix $G_* = [-u^{1*}, \ldots, -u^{m_*}]^T$ includes the undifferenced receiver-satellite unit direction vectors $u^{s_*^T}$ as its rows. The zenith-referenced standard deviation of the undifferenced code and phase observables are denoted as σ_{p_*} and σ_{ϕ_*}, respectively. $W_* = \text{diag}(w^{1*}, \ldots, w^{m_*})$ is the $m_* \times m_*$ diagonal matrix which captures the elevation-dependency of the GNSS observables. In this contribution, the satellite elevation-dependent weight w^{s_*} takes the form of the exponential weighting function as

$$w^{s_*} = [1 + 10 \exp(-\frac{\theta^{s_*}}{10})]^{-2} \tag{2}$$

where θ^{s_*} is the elevation of the satellite s_* in degrees (Euler and Goad, 1991). The unknowns to be estimated are the real-valued 3-vector of baseline increment b and the integer-valued $(m-1)$-vector of inter-system DD ambiguities a. Their corresponding single-epoch weighted least-squares float solutions, $\hat{b}$ and $\hat{a}$, are given as

$$\hat{b} = Q_{\hat{b}\hat{b}} G^T P_{D_m} Q_{pp}^{-1} p,\ Q_{\hat{b}\hat{b}} = (G^T P_{D_m} Q_{pp}^{-1} G)^{-1}$$

$$\hat{a} = \frac{1}{\lambda} D_m^T (\phi - G\hat{b}),\ Q_{\hat{a}\hat{a}} = \frac{1}{\lambda^2} D_m^T (Q_{\phi\phi} + G Q_{\hat{b}\hat{b}} G^T) D_m \tag{3}$$

with $P_{D_m} = D_m (D_m^T Q_{pp} D_m)^{-1} D_m^T Q_{pp}$. Since, in the case of a single epoch, the number of DD ambiguities equals that of the DD phase observables, uncorrelated with the DD code observables, the DD phase observables are fully reserved for the ambiguity estimation. Therefore, the single-epoch estimation of the baseline components does not benefit from the high precision phase observables unless the DD ambiguities are resolved to their integer values. Upon fixing the DD ambiguities, the phase observations act as the very precise code observations and improve the baseline estimation and precision. The fixed baseline estimation and its corresponding variance matrix are then given by

$$\check{b} = Q_{\check{b}\check{b}} G^T P_{D_m} (Q_{pp}^{-1} p + Q_{\phi\phi}^{-1} \phi)$$
$$Q_{\check{b}\check{b}} = (G^T P_{D_m} (Q_{pp}^{-1} + Q_{\phi\phi}^{-1}) G)^{-1} \tag{4}$$

To obtain the standalone IRNSS observational model from (1), it is enough to put $m_G = 0$. The redundancy and solvability for IRNSS and IRNSS+GPS are as follows

Fig. 1 CUCC (Left) and CUBB (Right) stations at Curtin University equipped with JAVAD TRE_G3TH_8 receivers, connected to TRM59800.00 SCIS antennas.

IRNSS	redundancy: $m_I - 4$ solvability: $m_I \geqslant 4$
IRNSS+GPS	redundancy: $m_I + m_G - 4$ solvability: $m_I + m_G \geqslant 4$

This implies that when the IRNSS is integrated with GPS, (1) would be solvable even if less than four satellites of each system are in view. Note that the redundancy and solvability of the IRNSS+GPS model would be different if the receivers are of different manufacturers and the ISBs are in turn present.

2.2 Height-Constrained Model

For some GNSS applications where the vertical position of the user does not vary considerably, information on the height component can be provided to strengthen the model of observations. Examples of such applications are bathymetric surveying (Zhu and Santerre, 2002), and kinematic positioning over small areas with low height fluctuations (Godha and Cannon, 2007). Enforcing a weighted height constraint, the observational model in (1) is extended with

$$E[\delta h] = [0,\ 0,\ 1]\, b; \qquad D[\delta h] = \sigma_h^2 \tag{5}$$

with δh being the height constraint corrected for an initial value of the height component, and σ_h the a priori standard deviation of the height constraint.

3 Measurement Set-Up

The data used in this study were taken from the two static stations CUBB and CUCC of a short baseline at Curtin University, Perth, Australia (Figure 1). Each station is equipped

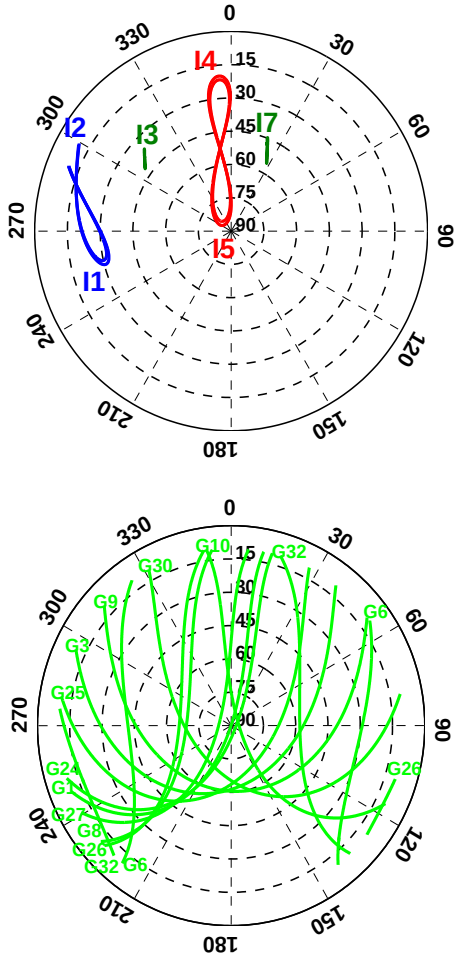

Fig. 2 The 24-hour skyplot of IRNSS (Top) and GPS Block IIF (Bottom) at Perth, Australia, on DOY 156 of 2016 with cut-off elevation of 10°.

with a JAVAD TRE_ G3TH_8 receiver and connected to a TRM59800.00 SCIS antenna. The data-set contains the 1-second IRNSS L5 and GPS L5 observations collected with a cut-off elevation angle of 10° on DOY (Day Of Year) 156 of 2016. Most of our analyses are conducted on an epoch-by-epoch basis and since the satellites geometry has a low rate of change over time, our conclusions would be valid even for lower sampling rates, like 30 seconds. For both constellations, the broadcast ephemeris is used. Figure 2 illustrates the 24-hour skyplot of IRNSS and GPS Block IIF at Perth.

3.1 Stochastic Properties

Prior to our analyses, we need to consider representative values for the zenith-referenced standard deviations in (1), i.e. $\{\sigma_{p_I}, \sigma_{\phi_I}, \sigma_{p_G}, \sigma_{\phi_G}\}$. These values will capture the measurement noise as well as any remaining mis-modeled effects like multipath. Therefore it is expected that upon eliminating the unwanted impact of multipath on the data, these values will experience improvement. The impact of multipath is eliminated using the method described in (Zaminpardaz et al, 2016a).

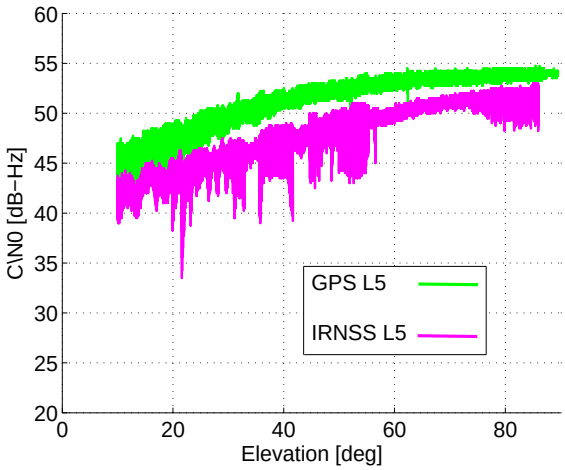

Fig. 3 Carrier-to-noise-density (C/N0) for IRNSS L5 and GPS Block IIF L5 signals tracked by a JAVAD TRE_G3TH_8 receiver, connected to a TRM59800.00 SCIS antenna at Perth, Australia, on DOY 156 of 2016.

Applying the least-squares variance component estimation (LS-VCE) (Teunissen and Amiri-Simkooei, 2008; Amiri-Simkooei et al, 2009) to the 1-second original and multipath-corrected data of DOYs 155 and 157 of 2016, the mentioned standard deviations were estimated and the corresponding results are given in Table 2. These estimations are obtained on the basis of baseline-known underlying model. The code precision of the GPS L5 is significantly better than that of the IRNSS L5. This is also in agreement with the signature of the carrier-to-noise-density (C/N0) graphs of the two systems in Figure 3. As it can be seen, the GPS L5-signal has larger values for C/N0 compared to the IRNSS L5, especially for elevations between 30° to 70°. After multipath reduction, both IRNSS and GPS code standard deviations improve significantly. The phase observables of IRNSS L5 and GPS L5 are of comparable precisions, and almost insensitive to the multipath correction. In the sequel, all our empirical analyses are based on the multipath-corrected data of the DOY 156 of 2016. In Table 2, the correlation coefficients of the phase and code observables for both IRNSS L5 and GPS L5 are also given. The small values for this quantity confirm that the two types of observations, phase and code, can be considered practically uncorrelated.

3.2 Time Correlation

As another aspect of the GNSS signals noise characteristics, here we assess the time correlation of the IRNSS and GPS

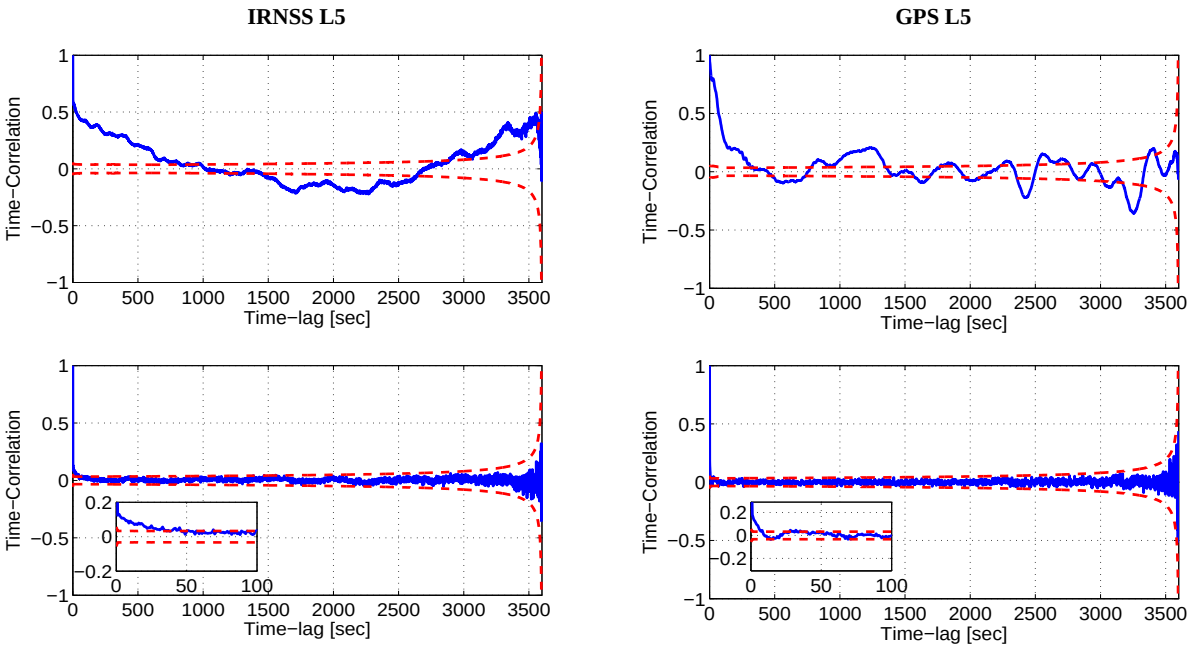

Fig. 4 Time series of the estimated time correlation among the short-baseline IRNSS L5 (Left) and GPS Block IIF L5 (Right) observations. [Top] Original data; [Bottom] Multipath-corrected data. The *red* dashed lines indicate the 95% formal confidence interval.

Table 2 LS-VCE estimation of the original and multipath-corrected (within brackets) undifferenced code σ_p and phase σ_ϕ zenith-referenced standard deviations and their corresponding correlation coefficient $\rho_{p\phi}$.

Frequency	σ_p [cm]	σ_ϕ [mm]	$\rho_{p\phi}$
IRNSS L5	26(19)	2(1)	-0.02(-0.01)
GPS L5	17(7)	1(1)	0.02(0.02)

L5 signals. This would be of importance when one is interested in multi-epoch processing. For this case, not only the correlation of the observations at a single epoch, but also their temporal correlation should properly be taken into account through the stochastic model. Figure 4 (top) shows the graph of the time correlation among the original IRNSS L5 and GPS L5 observations as function of their time difference, while Figure 4 (bottom) shows the same results for the multipath-corrected data. These graphs are based on applying the LS-VCE method to one hour of 1-second short-baseline data (Amiri-Simkooei and Tiberius, 2007). A significant time correlation of periodic behavior can be recognized among the original data for both the IRNSS and GPS observations. Upon removing the multipath effect however, the time correlation becomes negligible and the periodic signature vanishes. This means that when working with multipath-corrected data, they can safely be considered temporally uncorrelated even if the sampling rate is 1Hz.

3.3 Satellites Visibility and PDOP Analysis

Standalone IRNSS

The IRNSS constellation consists of seven satellites, three GEOs and four IGSOs. The 24-hour visibility of these satellites at Perth, on DOY 156 of 2016 with the cut-off angle of 10° is depicted in Figure 5 (in *gray*). As is shown, five and sometimes six satellites are visible from Perth. In addition to the number of satellites, Figure 5 also shows the time series of the corresponding PDOP (Position Dilution of Precision) which is defined as (Teunissen, 1998a; Hofmann-Wellenhof et al, 2013)

$$\text{PDOP} = \frac{1}{\sigma_{p_I}} \sqrt{\text{trace}\left(Q_{\hat{b}\hat{b}}\right)} \tag{6}$$

Since the IRNSS satellite geometry repeats itself every (solar) day four minutes earlier w.r.t. the previous day, the signature of the time series shown in Figure 5 is representable for any day.

The large values of PDOP during the 24-hour period demonstrate the poor IRNSS geometry for positioning. There exists one distinct peak in the PDOP time series at UTC [07:45:50]. Shown in Figure 6 is the skyplot of the IRNSS satellites at the mentioned time instant. As it can be seen, among the five visible satellites, two occupy the same skyplot position such that all five satellites form a cone-like geometry. Such a satellite geometry would in turn lead to the design matrix of the baseline b in (1) becoming rank defect, and PDOP getting large values. The design matrix $D_m^T G$ is

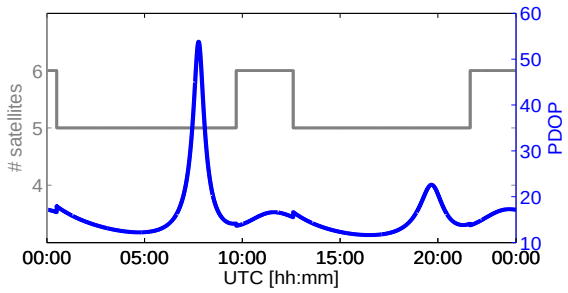

Fig. 5 Time series of the number of visible IRNSS satellites (*gray*) and their corresponding single-epoch PDOP (*blue*) at Perth, Australia on DOY 156 of 2016 with the cut-off angle of 10°.

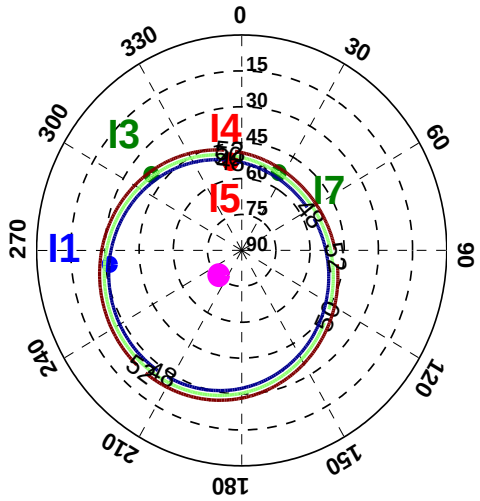

Fig. 6 IRNSS skyplot for Perth on DOY 156 of 2016 at UTC [07:45:50] with the cut-off angle of 10°. The *purple* dot denotes the symmetry axis d of the cone (cf. 8), i.e. the direction in which the receiver position is poorest estimable. The colored contour plots show the loci of unit vectors that make a constant angle of 48°, 50° and 52° with d.

rank defect if a vector $d \in \mathbb{R}^3$ can be found such that (Teunissen, 1990; Zaminpardaz et al, 2016b)

$$(D_m^T G)\, d \;=\; 0 \tag{7}$$

or equivalently

$$u^{s^T}\, d \;=\; \text{const}; \qquad s = 1, \ldots, m \tag{8}$$

implying that all the unit direction vectors from receiver to visible satellites, i.e. u^s $(s = 1, \ldots, m)$, make the same angle with the vector d. From a geometrical point of view, vector d is the symmetry axis of the cone on which the receiver-satellite unit direction vectors lie. The position solution becomes indeterminate in the direction of d. In the skyplot shown in Figure 6, the direction d is indicated as *purple* dot, and the corresponding cones as colored contour lines with the angles of 48°, 50° and 52°, respectively.

IRNSS integrated with GPS

Now consider the case when the IRNSS L5 observables are combined with the GPS L5. GPS Block IIF has 12 operational satellites of which the visibility at Perth is illustrated in Figure 7 (in *gray*). Combining IRNSS with GPS results in the number of visible satellites increasing from 5-6 to 6-11. The IRNSS+GPS PDOP (in *blue*) in Figure 7 demonstrates a considerable improvement compared to that of the standalone IRNSS (see Figure 5).

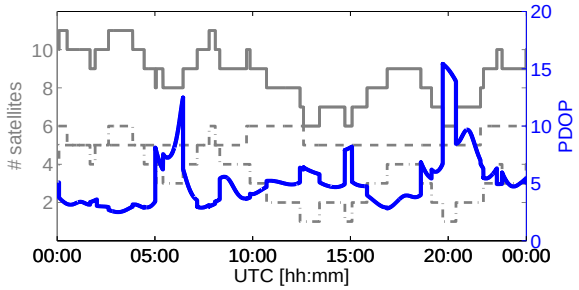

Fig. 7 Time series of the number of visible satellites of IRNSS (*gray* dashed line), of GPS Block IIF (*gray* dashed & dotted line), of both IRNSS and GPS Block IIF (*gray* solid line), and the corresponding single-epoch PDOP of IRNSS+GPS Block IIF (*blue*) at Perth, Australia on DOY 156 of 2016 with the cut-off angle of 10°.

4 Ambiguity Resolution

In this section, the IRNSS L5 ambiguity resolution performance is investigated. The impact of combining IRNSS L5 with GPS L5 observables on the ambiguity resolution will further be assessed. Our analyses will be based on the unconstrained, as well as height-constrained observational model. Note, the ambiguity resolution in this paper is conducted for the full vector of the DD ambiguities.

4.1 Ambiguity Dilution of Precision

The ambiguity dilution of precision (ADOP) was introduced in (Teunissen, 1997) as an easy-to-compute scalar diagnostic to measure the intrinsic model strength for successful ambiguity resolution. It is defined as the square root of the determinant of the ambiguity variance matrix raised to the power of one over the ambiguity dimension. Therefore, the single-baseline ADOP based on (3) is given as

$$\text{ADOP} \;=\; \sqrt{|Q_{\hat{a}\hat{a}}|}^{\frac{1}{m-1}} \tag{9}$$

The closed-form expression for the single-system ADOP, where the observations on the same frequency are of the

same quality, has already been provided in (Teunissen, 1997; Odijk and Teunissen, 2008), and the role of different factors such as receiver-satellite geometry and precision of the observables was investigated. As a rule-of thumb, an ADOP smaller than about 0.12 cycle corresponds to an ambiguity success rate, also known as the probability of correct integer estimation, larger than 99.9% (Odijk and Teunissen, 2008). An increase in the number of satellites would result in an improvement in the ADOP value. The magnitude of this improvement is even larger if the added satellite is from GPS Block IIF since the GPS L5 code observable is more precise than the IRNSS L5 (see Table 2).

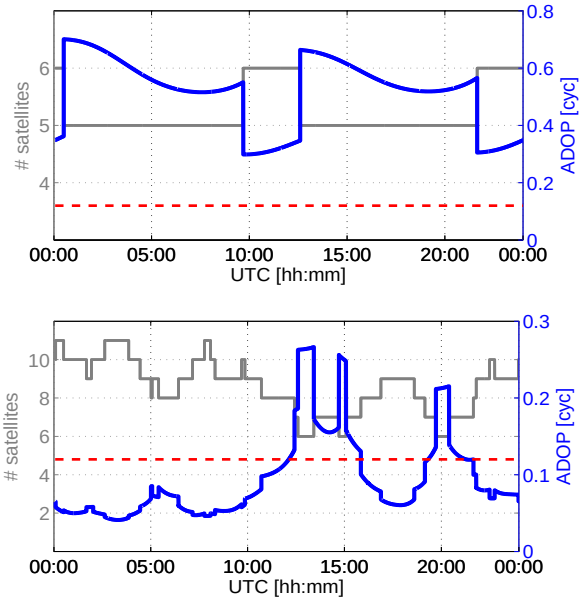

Fig. 8 Time series of the number of visible satellites (*gray*) and their corresponding single-epoch, single-baseline (CUBB-CUCC) ADOP (*blue*) for IRNSS (Top) and IRNSS+GPS Block IIF (Bottom) at Perth, Australia on DOY 156 of 2016 with the cut-off angle of 10°. The *red* dashed line indicates the ADOP value of 0.12 cycle.

Figure 8 shows the single-epoch ADOP time series of IRNSS (top) and IRNSS+GPS (bottom), as well as the corresponding number of visible satellites with the cut-off angle of 10° on DOY 156 of 2016. The horizontal *red* dashed line also indicates the ADOP value of 0.12 cycle. It can be seen that the fluctuations in the ADOP graphs resemble those in the graphs of the number of visible satellites. The standalone IRNSS ADOP ranges from 0.3-0.7 cycle which is by far more than the target value of 0.12 cycle. When the IRNSS is integrated with the GPS L5, the ADOP experiences a dramatic decrease particularly when more than one GPS satellite are in view.

4.2 From Unconstrained to Height-Constrained

Here, we assess, formally and empirically, the impact of (weighted) height-constraining on the ambiguity resolution performance by means of the ADOP and the success rate. Upon height-constraining with the standard deviation of σ_h, the ambiguities variance matrix improves as

$$Q_{\hat{a}\hat{a}|h} = Q_{\hat{a}\hat{a}} - \frac{1}{\sigma_h^2 + \sigma_{\hat{h}}^2} Q_{\hat{a}\hat{h}} Q_{\hat{h}\hat{a}} \tag{10}$$

Taking the determinant of both sides of the above equation and raising it to the power of $\frac{1}{2(m-1)}$, the weighted height-constrained ambiguity dilution of precision, denoted by $\mathrm{ADOP}_{|h}$, is given by

$$\begin{aligned} \mathrm{ADOP}_{|h} &= \mathrm{ADOP}\, \frac{\sigma_h^2/\sigma_{\hat{h}}^2 + \sigma_{\check{h}}^2/\sigma_{\hat{h}}^2}{\sigma_h^2/\sigma_{\hat{h}}^2 + 1} \\ &\approx \mathrm{ADOP}\, [1 + \sigma_{\hat{h}}^2/\sigma_h^2]^{-1} \end{aligned} \tag{11}$$

with $\sigma_{\hat{h}}$ and $\sigma_{\check{h}}$ being the standard deviations of, respectively, unconstrained float and fixed height solutions, and $Q_{\hat{a}\hat{h}}$ the unconstrained float ambiguity-height covariance. The approximation is due to the ratio $\sigma_{\check{h}}^2/\sigma_{\hat{h}}^2$ getting very small values, and is valid as long as $\sigma_{\check{h}}^2/\sigma_{\hat{h}}^2$ is negligible with respect to $\sigma_h^2/\sigma_{\hat{h}}^2$. This is the case when imposing a soft height constraint with relatively large value for σ_h. As (11) shows, the larger the ratio $\sigma_{\hat{h}}^2/\sigma_h^2$, the larger the ADOP improvement will be. Therefore, if σ_h^2 is much larger than $\sigma_{\hat{h}}^2$, the ambiguity resolution improvement brought by height-constraining would be negligible. Ambiguity resolution can benefit considerably from a weighted height constraint if $\sigma_{\hat{h}}^2$ is large. The larger $\sigma_{\hat{h}}^2$ is, the softer the weighted height constraint can be to still have an impact on ambiguity resolution. Thus, in case of a large $\sigma_{\hat{h}}^2$, soft constraining of the height can still result in a very significant improvement of ambiguity resolution. This is demonstrated in Figure 9.

The first row of Figure 9 shows the single-epoch float height standard deviation time series of the unconstrained model with 10° cut-off angle on DOY 156 of 2016, and the second to bottom rows present the corresponding ADOP time series for $\sigma_h = \infty$ (unconstrained), $\sigma_h = 1$m, $\sigma_h = 0.1$m and $\sigma_h = 0.01$m, respectively. Comparing the results of the standalone IRNSS (left column) with those of IRNSS+GPS (right column), the ADOP improvement after applying the weighted height constraint is overall larger for the standalone IRNSS. With the above explanation in mind, this is due to the larger values of $\sigma_{\hat{h}}$ of IRNSS compared to IRNSS+GPS. The results in the third row, especially those of standalone IRNSS, show that a soft height constraint of $\sigma_h = 1$m has a notable impact on ambiguity resolution at the time instances for which $\sigma_{\hat{h}}$ is large. Increasing the weight of the height constraint, the results of the fourth and fifth rows

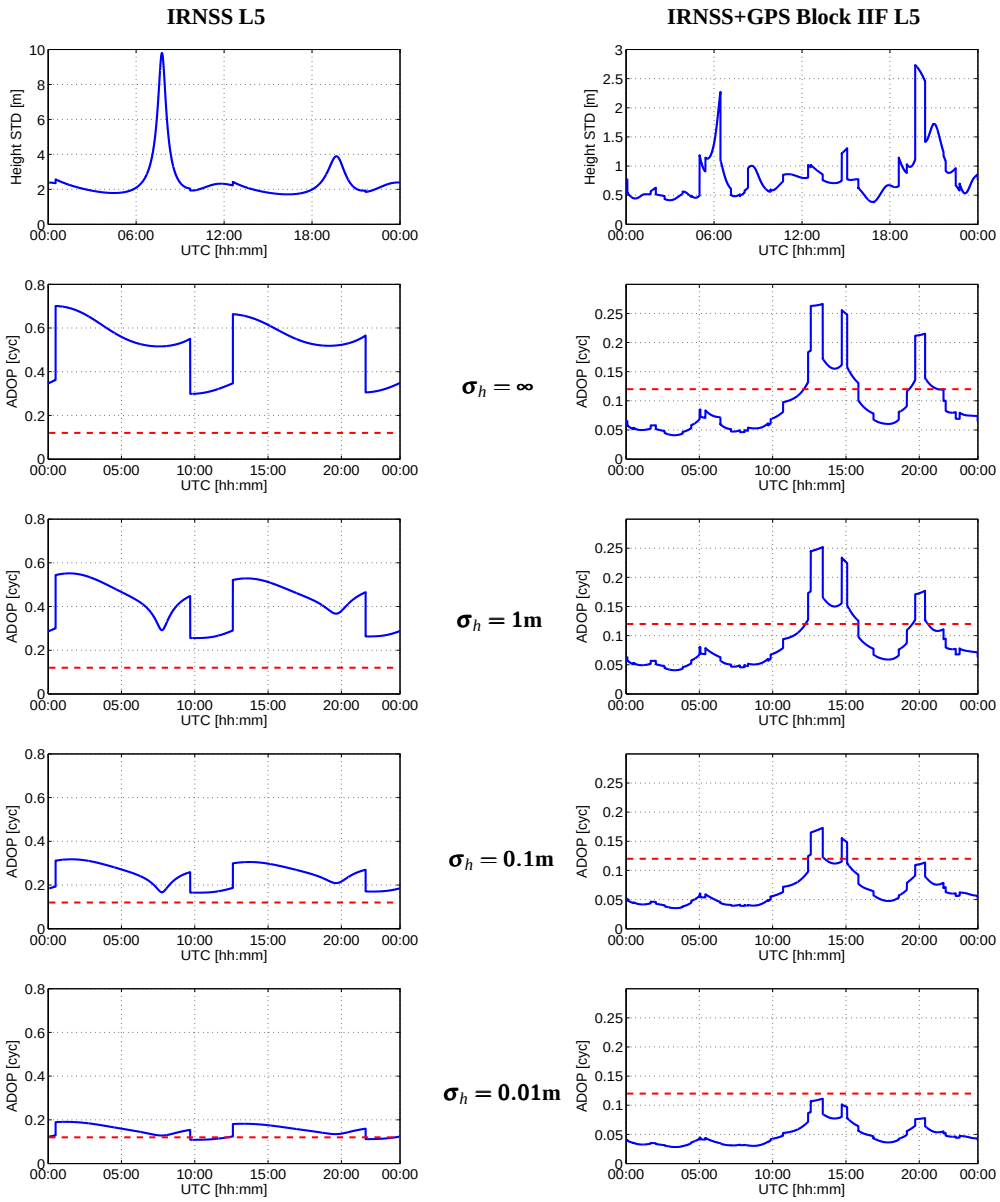

Fig. 9 [First row] Time series of the single-epoch unconstrained float height standard deviation of IRNSS L5 (Right) and IRNSS+GPS Block IIF L5 (Right) with the receiver pair CUBB-CUCC, on DOY 156 of 2016 with the cut-off angle of 10°. [From second row to bottom] The corresponding time series of the single-epoch ADOP based on the unconstrained ($\sigma_h = \infty$) and height-constrained model with the standard deviations of $\sigma_h = 1$m, $\sigma_h = 0.1$m and $\sigma_h = 0.01$m. The *red* dashed line indicates the ADOP value of 0.12 cycle.

of Figure 9 show that the ambiguity resolution improvements spread over to neighboring time instances. In case of a highly-weighted height constraint of $\sigma_h = 0.01$m, the ADOP of the combined systems is always smaller than 0.12 cycle, whereas the ADOP of the single-system IRNSS is mostly above the target value of 0.12 cycle.

Table 3 gives the single-epoch formal and empirical integer bootstrapped (IB) success rates as well as the empirical integer least-squares (ILS) success rate for the four models of Figure 9. The formal IB success rate is computed by taking the average of the 24-hour time series of the single-epoch IB success rate which is given as (Teunissen, 1998b)

$$\text{Formal IB } Ps = \prod_{i=1}^{m-1} \left[2\Phi\left(\frac{1}{2\sigma_{\hat{z}_{i|I}}} \right) - 1 \right] \tag{12}$$

where $\Phi(x) = \int_{-\infty}^{x} \frac{1}{\sqrt{2\pi}} \exp\{-\frac{1}{2}v^2\} dv$ and $\sigma_{\hat{z}_{i|I}}$ $(i = 1, \ldots, m-1$ and $I = 1, \ldots, m-2)$ are the conditional standard deviations of the *decorrelated* ambiguities. The reason behind choosing the bootstrapped success rate is two-fold. First it is easy to compute, and secondly it is the sharpest lower bound to the ILS success rate which has the highest success rate

Table 3 24-hour average single-epoch formal and empirical bootstrapped (IB) and empirical integer least-squares (ILS) success rate, for single- and dual-system scenarios, for the unconstrained model ($\sigma_h = \infty$) and the height-constrained model with different values for σ_h. emp: empirical; form: formal.

Model	IRNSS L5 *Ps* [%]			IRNSS+GPS Block IIF L5 *Ps* [%]		
	emp ILS	emp IB	form IB	emp ILS	emp IB	form IB
$\sigma_h = \infty$	19.7	19.5	19.9	97.5	97.4	97.1
$\sigma_h = 1$m	31.1	30.7	32.6	98.0	97.9	97.7
$\sigma_h = 0.1$m	70.8	70.3	73.2	99.2	99.2	99.2
$\sigma_h = 0.01$m	91.5	91.4	93.0	>99.9	>99.9	>99.9

of all admissible integer estimators (Teunissen, 1999; Verhagen and Teunissen, 2014). The empirical IB/ILS success rate is given as

$$\text{Empirical } Ps = \frac{\text{\# correct fixed DD ambiguities}}{\text{\# float DD ambiguities}} \tag{13}$$

To judge whether a DD ambiguity is correctly fixed, its corresponding IB/ILS solution is compared with the reference integer DD ambiguity computed based on the multi-epoch ILS solution of the baseline-known model. The empirical values in Table 3 are in good agreement with the formal ones, confirming the consistency between model and data. Also, the stronger the model is (from top to bottom), the larger the success rate becomes.

4.3 Ambiguity Resolution Performance Over the IRNSS Service Area

So far, we have presented the single-epoch ambiguity resolution formal and empirical analyses on the basis of the data collected at Perth. The consistency between our formal outcomes and their empirical counterparts implies that the easy-to-compute formal values can indeed be used to predict the expected ambiguity resolution performance. In this subsection, we conduct a formal analysis of the number of epochs needed to fix the DD ambiguities with the success rate of 99.9% over the IRNSS primary and secondary service area. Our analyses are valid for a short baseline such that the differential orbital and atmospheric errors can be neglected for. Figure 10 depicts the extent of these two areas as well as the locations chosen to be analysed in terms of ambiguity resolution performance (*red*: primary locations; *black*: secondary locations). Since ambiguities remain constant over time (in case of no loss-of-lock or cycle slip), the ambiguity resolution performance can improve if this time-constancy is taken into account through a Kalman filter. The number of epochs needed to fix the DD ambiguities is then computed as follows

1. Initialize filter with the data of a single epoch.
2. Compute the DD ambiguities variance matrix.

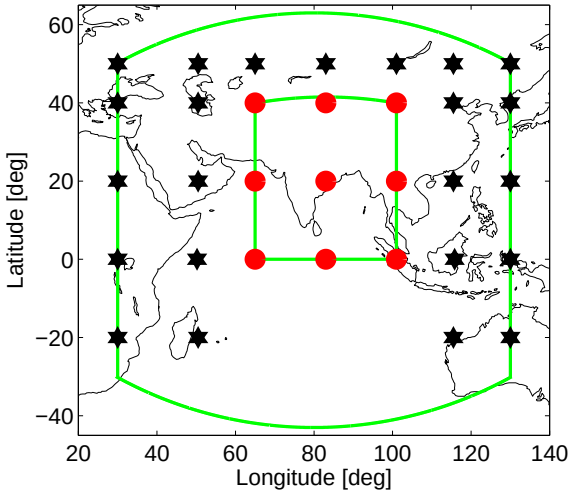

Fig. 10 IRNSS primary (*red* circles) and secondary (*black* hexagrams) service area locations. The inner and outer *green* boundaries indicate the border of the primary and secondary service areas, respectively.

3. Compute the bootstrapped success rate *Ps* based on the decorrelated DD ambiguities (cf. 12).
4. If $Ps < 99.9\%$, go to step 5, otherwise quit the loop.
5. Accumulate the data of the next epoch and go to step 2.

Providing a 24-hour time series of the number of epochs needed to fix the DD ambiguities, we make use of the boxplot concept to give the statistical properties of this time series. Note that as 30-second is the most common sampling rate in GNSS community, our results here are provided on the basis of such a sampling rate. To be conservative, the code standard deviation that we use for GPS L5-signal is $\sigma_{p_G} = 20$cm (Nadarajah et al, 2015) and for IRNSS L5-signal is $\sigma_{p_I} = 30$cm, which is considered less precise than the GPS L5-signal (see Table 2). The phase standard deviation for both systems is considered as $\sigma_{\phi_I} = \sigma_{\phi_G} = 1$mm.

Figure 11 for the standalone IRNSS L5, and Figure 12 for the IRNSS+GPS Block IIF L5, show the boxplots of the number of epochs to fix the ambiguities. Each panel contains the results of both kinematic and static scenarios separated with a vertical *gray* line. To the left of this line are shown the unconstrained and height-constrained ($\sigma_h = 1$m) kinematic boxplots, and to the right their static counterparts. In each boxplot, the horizontal lines from bottom to top show: 2^{nd} percentile (*black*), 25^{th} percentile (*blue*), 50^{th} percentile (*green*), 75^{th} percentile (*blue*) and 98^{th} percentile (*black*) of the mentioned time series, and *red* pluses show the remaining values thereof.

We first consider the IRNSS standalone results. It can be seen that for those locations on the equator ($\phi = 0^\circ$, $55.5^\circ < \lambda < 115.5^\circ$), the ambiguity resolution performance is almost independent from the underlying model being kinematic or

static, unconstrained or height-constrained. This conclusion is also valid for the locations ($\phi = 20^\circ,\ 65^\circ < \lambda < 101^\circ$). The performance of the unconstrained and height-constrained static ambiguity resolution are similar for all the locations. This is due to the fact that the multi-epoch static height standard deviation $\sigma_{\hat{h}}$ is so small such that a soft height constraint with $\sigma_h = 1$m does not bring any considerable improvement to the ambiguity resolution performance (see Figure 9). As one goes further away from the central location ($\phi = 0^\circ,\ \lambda = 83^\circ$), the ambiguity resolution performance gets poorer. Excluding the locations within ($0^\circ < \phi < 20^\circ,\ 65^\circ < \lambda < 101^\circ$), the IRNSS user needs a considerably long time to fix the DD ambiguities with $Ps = 99.9\%$.

We repeated our analysis of the required number of epochs to fix the DD ambiguities for a higher sampling rate of 1-second, as well. Although the number of epochs increases, the period length needed to achieve a success rate of $Ps = 99.9\%$ decreases dramatically. As an example, we consider the unconstrained kinematic results of the location ($\phi = -20^\circ,\ \lambda = 115.5^\circ$). Switching from 30-second to 1-second sampling rate, the 2^{nd}, 25^{th}, 50^{th}, 75^{th} and 98^{th} percentile experience the following changes respectively: $4(120\text{sec}) \rightarrow 5(5\text{sec})$, $7(210\text{sec}) \rightarrow 8(8\text{sec})$, $13(390\text{sec}) \rightarrow 20(20\text{sec})$,-$20(600\text{sec}) \rightarrow 29(29\text{sec})$ and $42(1260\text{sec}) \rightarrow 79(79\text{sec})$. This means that in case of using the high sampling rate of 1-second, one needs a dramatically shorter time period to achieve $Ps = 99.9\%$ w.r.t. using 30-second data.

Integration of IRNSS with the GPS Block IIF brings a huge benefit to the users within the IRNSS service area, especially for those on the border of the secondary service area. The median (50^{th} percentile) for all the locations is now one to two epochs, and the difference between various percentiles reduces, meaning that the variability of the number of epochs over the 24-hour period has reduced. As Figure 12 shows, (almost) instantaneous ambiguity resolution is feasible during the whole day for those locations within ($0^\circ < \phi < 20^\circ,\ 65^\circ < \lambda < 101^\circ$).

GPS Block IIF is the first generation of GPS with the capability of transmitting L5 signal, and the next GPS generation, GPS III, will also be transmitting L5 signal as well (Marquis and Shaw, 2016). GPS III is planned to become fully operational with a constellation of 32 satellites by 2025 (Lockheed Martin, 2013; Bensky, 2016), and the first launch thereof is expected in 2017 (GPS World, 2016). For the situation when the GPS III has reached its full operational capability, we computed the required number of epochs for fixing the L5 DD ambiguities using single-system GPS III and dual-system IRNSS+GPS III. In case of the single-system GPS III, the 24-hour instantaneous ambiguity resolution with $Ps = 99.9\%$ is not feasible for any of the locations within the IRNSS service area. As to the dual-system IRNSS+GPS III however, our computations show that for the required success rate of $Ps = 99.9\%$ and even of $Ps = 99.99\%$, *instantaneous ambiguity resolution* becomes always feasible for all the locations within the IRNSS service area. This is also consistent with the results presented by (Odolinski and Teunissen, 2016). There, the performance of the dual-system single-frequency is compared with that of the single-system dual-frequency, and it is shown that for these scenarios, comparable ambiguity resolution performance are achievable and instantaneous ambiguity-resolved positioning is always feasible. Note that our computations are based on $\sigma_{p_G} = 20$cm. Since the GPS III signals would be three times more accurate than the current GPS signals (Marquis and Shaw, 2016), IRNSS+GPS III L5 instantaneous ambiguity resolution even with success rates higher than 99.99% may become achievable.

5 Positioning Results

In this section, the single-epoch positioning results for IRNSS and then for IRNSS+GPS are presented. The underlying model ranges from unconstrained to highly-weighted height-constrained model.

5.1 Standalone IRNSS

Shown in Figure 13 is the standalone IRNSS L5 unconstrained single-epoch float horizontal scatter plot for the CUBB-CUCC baseline on DOY 156 of 2016. As it can be seen, there exist some excursions in the scatter plot which correspond with that time interval with large PDOPs (see Figure 5). In addition, the formal and empirical 95% confidence ellipses are also illustrated by, respectively, *blue* and *purple* colors, showing a good consistency. Note that the formal and empirical confidence ellipses are computed on the basis of the respective formal and empirical variance matrix. Formal variance matrix is obtained from taking the average of all the single-epoch least-squares baseline variance matrices. Whereas, the empirical variance matrix is obtained from the differences of the estimated baseline and the available ground truth of the CUBB-CUCC baseline.

Note that the scatter plot and the confidence ellipses are elongated in almost North-Westerly direction. This can be explained by means of the receiver-satellite geometry and its impact on the confidence ellipse of $\hat{b}$,

$$(\hat{b} - b)^T Q_{\hat{b}\hat{b}}^{-1} (\hat{b} - b) \;=\; r^2 \tag{14}$$

in which the constant r^2 is chosen such that a certain confidence level is reached. As the direction of elongation is given by the direction of the eigenvector of $Q_{\hat{b}\hat{b}}^{-1}$ corresponding to its smallest eigenvalue, it follows with the aid of (3)

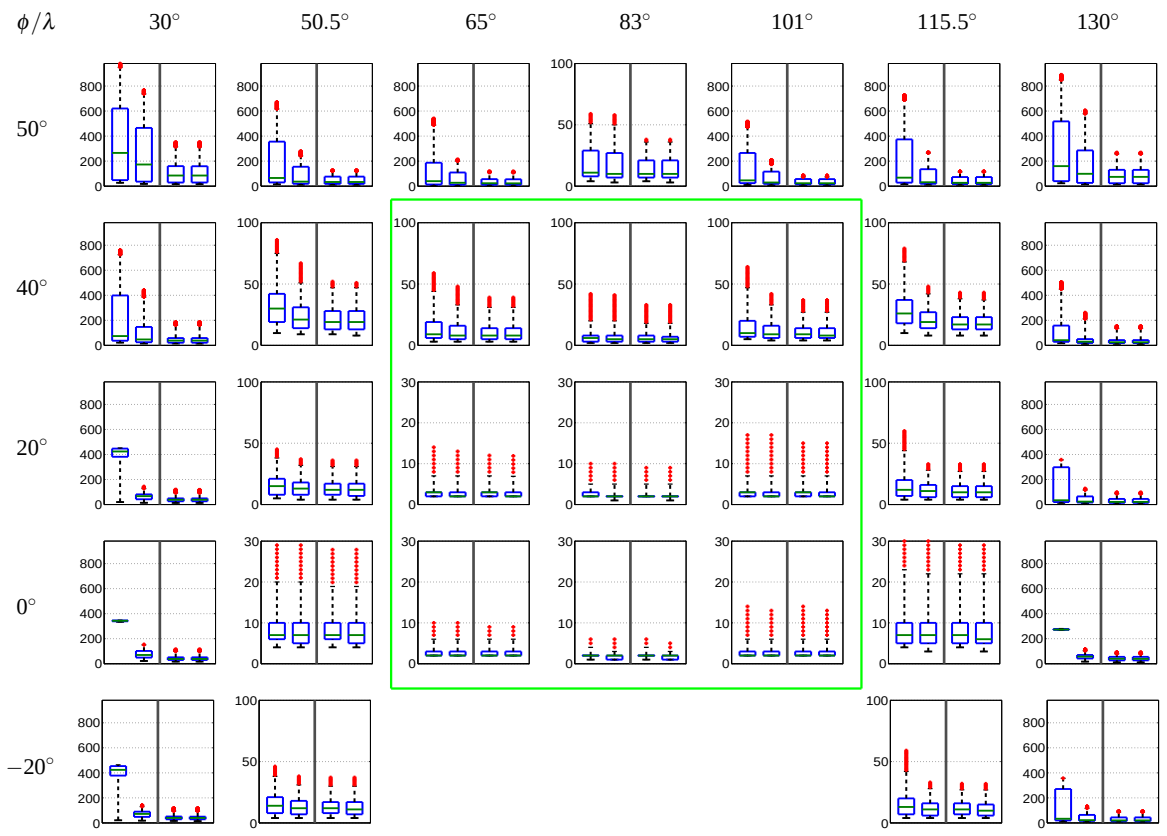

Fig. 11 Boxplots of the standalone IRNSS L5 time series of the required number of epochs to fix the DD ambiguities with $Ps > 99.9\%$ using 30-second sampling rate over the IRNSS service area, on DOY 156 of 2016 with the cut-off angle of 10°. The primary service area is located within the *green* border. Each panel shows four boxplots corresponding with different underlying models: from left to right, the kinematic unconstrained and height-constrained ($\sigma_h = 1$m) and static unconstrained and height-constrained ($\sigma_h = 1$m) model, respectively. In each boxplot, the horizontal lines from bottom to top show: 2^{nd} percentile (*black*), 25^{th} percentile (*blue*), 50^{th} percentile (*green*), 75^{th} percentile (*blue*) and 98^{th} percentile (*black*) of the mentioned time series, and *red* pluses show the remaining values thereof. These boxplots are computed based on $\sigma_{p_I} = 30$cm and $\sigma_{\phi_I} = 1$mm.

Table 4 Standalone IRNSS L5 single-epoch empirical and formal standard deviations of the CUBB-CUCC baseline float and fixed estimations on DOY 156 of 2016 with the cut-off elevation angle of 10°. The underlying models are unconstrained ($\sigma_h = \infty$) and height-constrained for $\sigma_h = 1,\ 0.1,\ 0.01$m. $\sigma_{\hat{n}}/\sigma_{\check{n}}$: north standard deviation; $\sigma_{\hat{e}}/\sigma_{\check{e}}$: east standard deviation; $\sigma_{\hat{h}}/\sigma_{\check{h}}$: height standard deviation.

		$\sigma_h = \infty$		$\sigma_h = 1$ m		$\sigma_h = 0.1$ m		$\sigma_h = 0.01$ m	
		empirical	formal	empirical	formal	empirical	formal	empirical	formal
Float	$\sigma_{\hat{n}}$ [m]	1.48	1.44	1.11	1.09	1.01	1.01	1.01	1.01
	$\sigma_{\hat{e}}$ [m]	1.04	1.05	0.73	0.74	0.65	0.66	0.65	0.66
	$\sigma_{\hat{h}}$ [m]	2.56	2.71	0.89	0.91	0.10	0.10	0.01	0.01
	$\rho_{\hat{n}\hat{e}}$	-0.64	-0.62	-0.57	-0.58	-0.49	-0.52	-0.49	-0.52
	$\rho_{\hat{n}\hat{h}}$	0.33	0.30	0.33	0.30	0.04	0.04	0.00	0.00
	$\rho_{\hat{e}\hat{h}}$	-0.72	-0.72	-0.45	-0.43	-0.05	-0.05	0.00	0.00
Fixed	$\sigma_{\check{n}}$ [m]	–	–	–	–	0.007	0.005	0.006	0.005
	$\sigma_{\check{e}}$ [m]	–	–	–	–	0.005	0.004	0.005	0.003
	$\sigma_{\check{h}}$ [m]	–	–	–	–	0.010	0.010	0.007	0.006
	$\rho_{\check{n}\check{e}}$	–	–	–	–	-0.70	-0.61	-0.74	-0.65
	$\rho_{\check{n}\check{h}}$	–	–	–	–	0.28	0.28	0.44	0.42
	$\rho_{\check{e}\check{h}}$	–	–	–	–	-0.67	-0.72	-0.61	-0.64

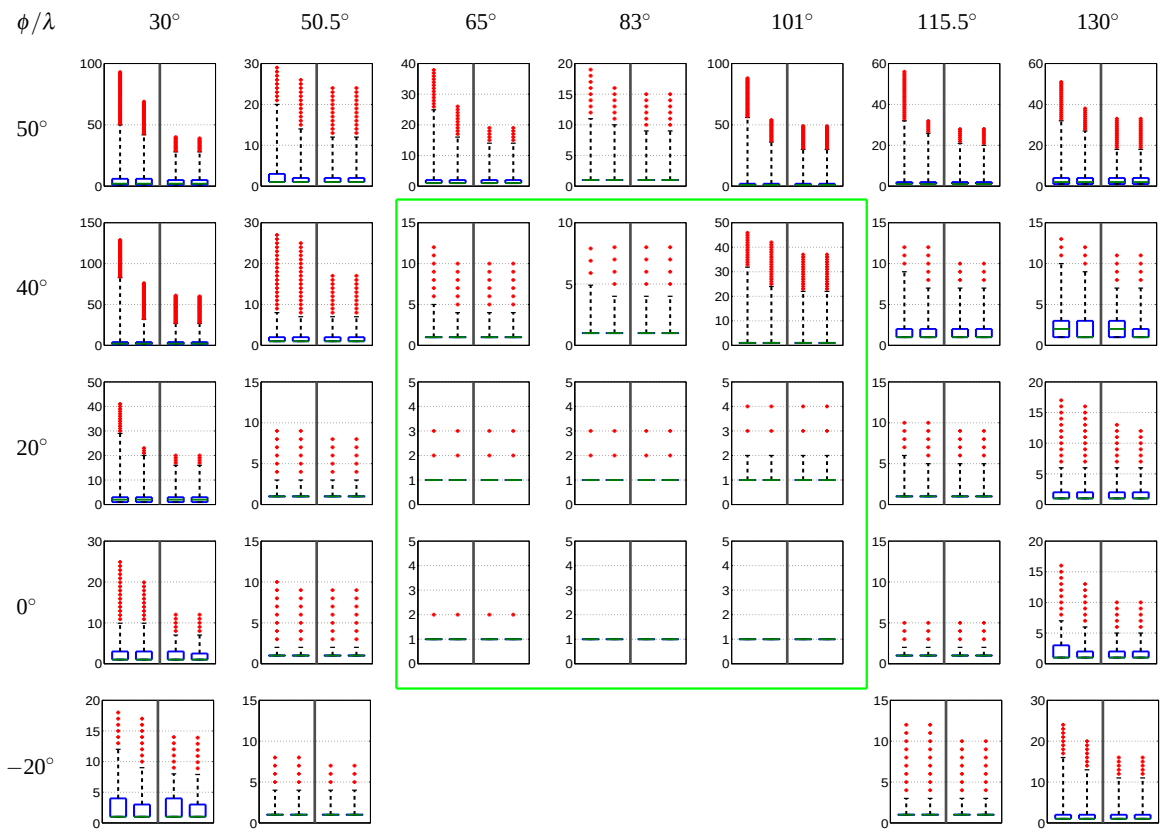

Fig. 12 Boxplots of the IRNSS+GPS Block IIF L5 time series of the required number of epochs to fix the DD ambiguities with $Ps > 99.9\%$ using 30-second sampling rate over the IRNSS service area, on DOY 156 of 2016 with the cut-off angle of 10°. The primary service area is located within the *green* border. Each panel shows four boxplots corresponding with different underlying models: from left to right, the kinematic unconstrained and height-constrained ($\sigma_h = 1$m) and static unconstrained and height-constrained ($\sigma_h = 1$m) model, respectively. In each boxplot, the horizontal lines from bottom to top show: 2^{nd} percentile (*black*), 25^{th} percentile (*blue*), 50^{th} percentile (*green*), 75^{th} percentile (*blue*) and 98^{th} percentile (*black*) of the mentioned time series, and *red* pluses show the remaining values thereof. These boxplots are computed based on $\sigma_{p_I} = 30$cm, $\sigma_{p_G} = 20$cm and $\sigma_{\phi_I} = \sigma_{\phi_G} = 1$mm.

that this direction is given by

$$\begin{aligned} f &= \underset{\tilde{f}}{\operatorname{argmin}}\ \tilde{f}^T Q_{\hat{b}\hat{b}}^{-1} \tilde{f} \\ &= \underset{\tilde{f}}{\operatorname{argmin}} \sum_{s=1}^{m} w^s [\tilde{f}^T (u^s - \bar{u})]^2 \end{aligned} \tag{15}$$

Figure 14 depicts the day-averaged skyplot position of the IRNSS satellites as well as that of the weighted-average $\bar{u}$ at Perth on DOY 156 of 2016 with the cut-off angle of 10°. As the differences $(u^s - \bar{u})$ are mainly oriented along the North-East direction, the direction f that minimizes their contribution to (15) will mainly lie in a North-Westerly direction.

Table 4 lists the standalone IRNSS single-epoch formal and empirical standard deviations and correlation coefficients of the CUBB-CUCC baseline components for both ambiguity-float and ambiguity-fixed scenarios. The fixed results are only given for the models with success rates more than 70% (see Table 3). As σ_h gets smaller from $\sigma_h = \infty$ to $\sigma_h = 0.1$m, the baseline estimation gets better in precision. However, from $\sigma_h = 0.1$m to $\sigma_h = 0.01$m no further precision improvement can be achieved for the north and east components.

5.2 IRNSS Integrated with GPS

Integrating IRNSS L5 with GPS L5 observations, Table 5 presents the single-epoch empirical and formal standard deviations and correlation coefficients of the CUBB-CUCC baseline components for ambiguity-float scenario. Comparing the results in this table with those in Table 4, the baseline estimation precision improves by a factor of 4-5 horizontally and 2-3 vertically. Imposing a height constraint indeed improves the baseline float solution precision, but not as much as it does for the standalone IRNSS. This is due to the fact that the combined system is stronger than the single system, and thus experiencing less improvement caused by height-constraining. Upon fixing the DD ambiguities, the very precise phase observations take the leading role in baseline esti-

Table 5 IRNSS+GPS Block IIF L5 single-epoch empirical and formal standard deviations of the CUBB-CUCC baseline float estimations on DOY 156 of 2016 with the cut-off angle of 10°. The underlying models are unconstrained ($\sigma_h = \infty$) and height-constrained for $\sigma_h = 1,\ 0.1,\ 0.01$m. $\sigma_{\hat{n}}$: north standard deviation; $\sigma_{\hat{e}}$: east standard deviation; $\sigma_{\hat{h}}$: height standard deviation.

		$\sigma_h = \infty$		$\sigma_h = 1$ m		$\sigma_h = 0.1$ m		$\sigma_h = 0.01$ m	
		empirical	formal	empirical	formal	empirical	formal	empirical	formal
Float	$\sigma_{\hat{n}}$ [m]	0.30	0.34	0.29	0.31	0.26	0.28	0.26	0.28
	$\sigma_{\hat{e}}$ [m]	0.37	0.40	0.31	0.35	0.28	0.31	0.28	0.31
	$\sigma_{\hat{h}}$ [m]	0.82	0.93	0.54	0.61	0.10	0.10	0.01	0.01
	$\rho_{\hat{n}\hat{e}}$	-0.24	-0.22	-0.17	-0.17	-0.13	-0.15	-0.13	-0.15
	$\rho_{\hat{n}\hat{h}}$	0.23	0.23	0.16	0.16	0.03	0.03	0.00	0.00
	$\rho_{\hat{e}\hat{h}}$	-0.46	-0.45	-0.23	-0.24	-0.03	-0.03	0.00	0.00

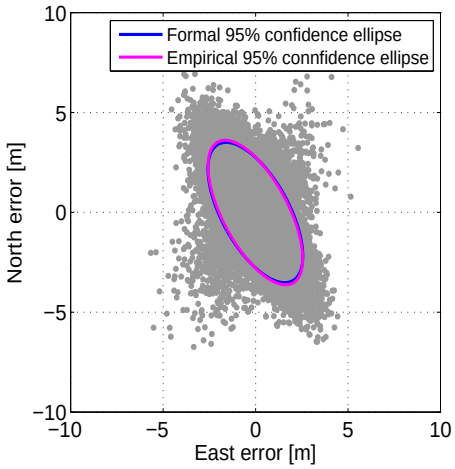

Fig. 13 Standalone IRNSS L5 unconstrained single-epoch float horizontal baseline scatter plot corresponding with receiver pair CUBB-CUCC on DOY 156 of 2016 with the cut-off angle of 10°. The *blue* and *purple* ellipses show, respectively, the 95% formal and empirical confidence ellipses.

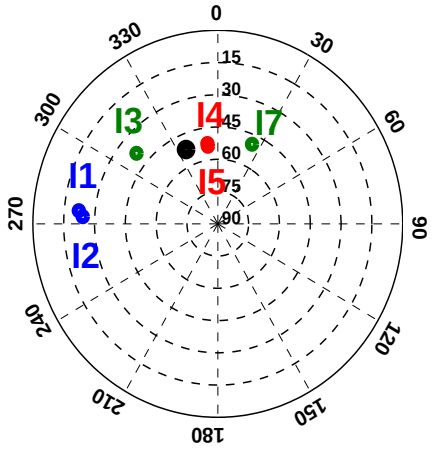

Fig. 14 Day-averaged IRNSS skyplot at Perth for DOY 156 of 2016 with the cut-off angle of 10°. The *black* dot indicates the skyplot position of vector $\bar{u}$ (cf. 15).

mation. In case of $\sigma_{p_I} = \sigma_{p_G}$ and $\sigma_{\phi_I} = \sigma_{\phi_G}$, the fixed baseline standard deviations improve by a factor of $\sigma_{p_I}/\sigma_{\phi_I}$ w.r.t. their float counterparts. However, from Table 2, $\sigma_{p_I} \neq \sigma_{p_G}$, and the ratio of code and phase standard deviations is 190 for IRNSS L5 and 70 for GPS L5. The improvement that is achieved upon fixing the DD ambiguities is around a factor of 150, which lies between 70 and 190. For the chosen values of σ_h, the fixed solutions are almost insensitive to height-constraining. That is because the height-constraining does not bring any considerable benefit to a model which is already strong enough.

Figure 15 depicts the unconstrained single-epoch 1-second horizontal scatter plot (Top) and height time series (Middle) of the CUBB-CUCC baseline float solutions (in *gray*), correctly fixed solutions (in *green*) and wrongly fixed solutions (in *red*), and the corresponding ADOP time series (Bottom) on the basis of L5 observables of IRNSS and GPS Block IIF collected on DOY 156 of 2016 with the cut-off angle of 10°. The scatter plot is of non-ellipsoidal shape which is due to the significant changes that the receiver-satellite geometry undergoes during the whole day.

Inside the middle panel is also shown the 95% formal confidence interval based on the float height standard deviation of which the signature is in good agreement with that of the height error time series, confirming the consistency between data and model. Comparing the time series of the height solution with that of the ADOP, the wrong ambiguity fixing occurs during the periods of large ADOPs. It can also be seen that despite large fluctuations in float height solution during for example UTC [05:00-07:00], DD ambiguities can be correctly fixed. This indicates that while a receiver-satellite geometry can be poor for positioning, it can still be strong enough for ambiguity resolution (Teunissen et al, 2014; Zaminpardaz et al, 2016a).

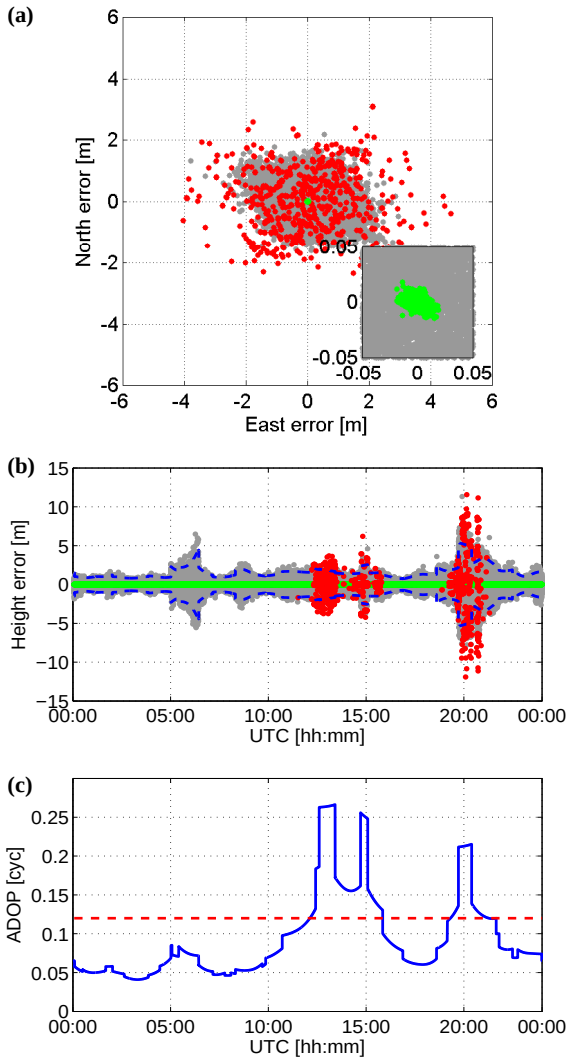

Fig. 15 (a) IRNSS+GPS Block IIF L5 unconstrained single-epoch horizontal baseline scatter plot corresponding with receiver pair CUBB-CUCC on DOY 156 of 2016 with the cut-off angle of 10°. *gray*: float solution; *green*: correctly fixed solution; *red*: wrongly fixed solution (b) The corresponding time series of the height component. The *blue* dashed lines indicate the 95% formal confidence interval. (c) The corresponding time series of the single-epoch ADOP (*blue*) and the target value of 0.12 cycle (*red* dashed line).

5.3 Positioning Performance Over the IRNSS Service Area

The positioning results presented in the previous subsection reveal that the formal values are indeed reliable representatives for their empirical counterparts. Therefore, in this subsection, we provide a formal analysis of the positioning performance over the IRNSS service area. For our analyses, we chose two stations within the primary service area, namely ($\phi = 0^\circ,\ \lambda = 83^\circ$) and ($\phi = 40^\circ,\ \lambda = 65^\circ$). The rationale behind choosing these two locations is two-fold. First, their positioning performance are quite different and secondly, the instantaneous ambiguity resolution is feasible over these two locations when integrating IRNSS with GPS.

Figure 16 shows the number of visible satellites (in *black*) with the cut-off angle of 10°, unconstrained single-epoch north and east standard deviations (in *blue*) and correlation coefficient (in *gray*) time series for ($\phi = 0^\circ,\ \lambda = 83^\circ$) to the top and for ($\phi = 40^\circ,\ \lambda = 65^\circ$) to the bottom. The underlying model varies, from left to right, from standalone IRNSS to IRNSS+GPS Block IIF to IRNSS+GPS III. Again to be conservative we set $\sigma_{p_I} = 30$cm, $\sigma_{p_G} = 20$cm and $\sigma_{\phi_I} = \sigma_{\phi_G} = 1$mm. As the model gets stronger from left to right, the level of standard deviations decreases. The east standard deviation shows a rather stable behavior for all the cases, and this is due to that fact that the IRNSS satellites geometry for the mentioned two locations has a large extent along the East-West direction. The north standard deviation stabilizes as well provided that the IRNSS is integrated with GPS III.

As Figure 12 shows, ambiguity resolution can be conducted instantaneously always at ($\phi = 0^\circ,\ \lambda = 83^\circ$) and most of the time at ($\phi = 40^\circ,\ \lambda = 65^\circ$), when integrating IRNSS L5-signal with GPS Block IIF L5-signal. The corresponding fixed north and east standard deviations, given $\sigma_{p_I} = 30$cm, $\sigma_{p_G} = 20$cm, $\sigma_{\phi_I} = \sigma_{\phi_G} = 1$mm, becomes around 250 times better than their float counterparts in Figure 16 (middle). As was mentioned earlier, when the GPS III with the capability of transmitting L5 signals becomes fully operational, the 24-hour instantaneous ambiguity-resolved positioning would be realized for all the locations within the IRNSS service area upon integration of IRNSS with GPS III.

6 Summary and Concluding Remarks

In this contribution, for the fully-operational IRNSS as a standalone system and also in combination with GPS, we provided an initial assessment of L5 integer ambiguity resolution and positioning performance. We studied the noise characteristics of the L5-signal for both IRNSS and GPS through carrier-to-noise density, measurement precision and time correlation. The results show that the GPS data have a significantly lower noise level than that of IRNSS, particularly in case of the code data. Also the time correlation of both the constellations can be neglected provided that the multipath impact is corrected for, even if 1-second data are used. We therefore based all our empirical analyses of ambiguity resolution and positioning on the multipath-corrected 1-second data collected by two stations at Perth.

Using real data, single-epoch L5 ambiguity resolution performance was assessed by means of two scalar measures: ambiguity dilution of precision (ADOP) and easy-to-compute bootstrapped success rate, in the framework of unconstrained/

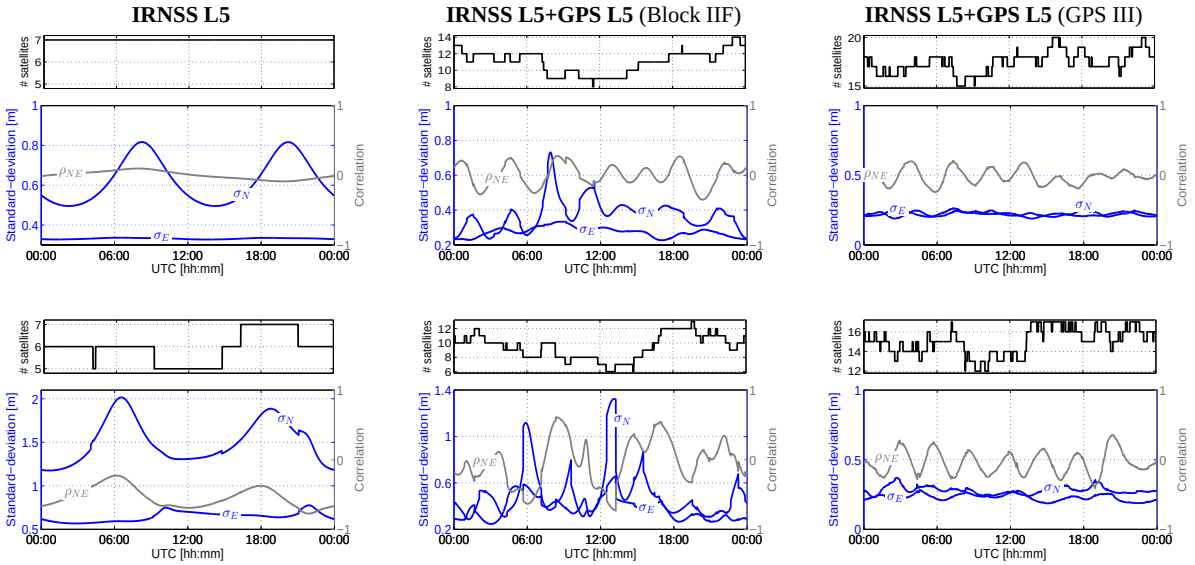

Fig. 16 Time series of the number of visible satellites (*black*), unconstrained single-epoch float east and north standard deviations (*blue* curves) and their corresponding correlation coefficient (*gray* curve) on DOY 156 of 2016 with the cut-off angle of 10° for locations (top row) $\phi = 0°,\ \lambda = 83°$ and (bottom row) $\phi = 40°,\ \lambda = 65°$. These graphs are computed based on $\sigma_{p_I} = 30$cm, $\sigma_{p_G} = 20$cm and $\sigma_{\phi_I} = \sigma_{\phi_G} = 1$mm.

height-constrained and single-system/dual-system. Integrating the IRNSS with GPS Block IIF, ADOP experiences a dramatic decrease particularly when more than one GPS satellite are in view. We also compared empirical and formal success rates for the mentioned underlying models, thereby showing the consistency between data and models.

The agreement between our empirical outcomes and their formal counterparts implies that the easy-to-compute formal values can indeed be used to predict the expected ambiguity resolution performance. We conducted a formal analysis of the number of epochs needed to fix the DD ambiguities with the success rate of 99.9% over the IRNSS primary and secondary service area. Providing a 24-hour time series of the number of epochs, we made use of the boxplot concept to give the statistical properties of this time series. The underlying model varied from single-system IRNSS to dual-system IRNSS+GPS, from unconstrained to height-constrained ($\sigma_h = 1$m), and from kinematic to static. As to the standalone IRNSS, our results showed that as one goes further away from the IRNSS constellation central location ($\phi = 0°,\ \lambda = 83°$), the ambiguity resolution performance gets poorer. Excluding the locations within ($0° < \phi < 20°,\ 65° < \lambda < 101°$), the IRNSS user needs a considerably long time to fix the DD ambiguities with $Ps = 99.9\%$. This time period can notably decrease if one employs higher sampling rates.

Integration of IRNSS with the GPS Block IIF brings a huge benefit to the users within the IRNSS service area, especially for those on the border of the secondary service area, such that the median for all the locations becomes one to two epochs, and the variability of the number of epochs over the 24-hour period reduces. For this case, (almost) instantaneous ambiguity resolution is feasible during the whole day for those locations within ($0° < \phi < 20°,\ 65° < \lambda < 101°$). For the case when the fully-operational GPS III with the capability of transmitting L5 signal has been realized, we computed the required number of epochs for fixing the DD ambiguities with $Ps = 99.9\%$ and $Ps = 99.99\%$ using IRNSS+GPS III. Our computations showed that instantaneous ambiguity resolution for both the values of success rate becomes always feasible for all the locations within the IRNSS service area.

Next to the ambiguity resolution performance, we also investigated the positioning capability of standalone IRNSS (L5) and IRNSS+GPS (L5). All the empirical and formal values were in agreement with each other, further confirming the consistency between data and model. While the scatter plot corresponding with single-system IRNSS looked ellipsoidal, that corresponding with IRNSS+GPS Block IIF (L5) was non-ellipsoidal due to the significant change in receiver-satellite geometry. Integrating IRNSS L5 with GPS Block IIF L5 observations improved the baseline estimation precision considerably w.r.t. standalone IRNSS L5. Comparing the time series of the fixed height solution with that of the ADOP, the wrong ambiguity fixing occurs during the periods of large ADOPs. We also showed despite large fluctuations in float height solution, DD ambiguities can be correctly fixed. This indicates that while a receiver-satellite geometry can be poor for positioning, it can be strong enough for ambiguity resolution. Finally, we provided a formal analysis of the positioning performance for two stations within the primary service area. The underlying model varied from IRNSS (L5) to IRNSS+GPS Block IIF (L5) to IRNSS+GPS

III (L5). As the model gets stronger, the level of standard deviations decreases and their time series stabilizes.

Acknowledgment This work has been done in the context of the Positioning Program Project 1.19 “Multi-GNSS PPP-RTK Network” of the Cooperative Research Centre for Spatial Information (CRC-SI). The second author is the recipient of an Australian Research Council (ARC) Federation Fellowship (project number FF0883188).

References

Amiri-Simkooei AR, Tiberius CCJM (2007) Assessing receiver noise using GPS short baseline time series. GPS solutions 11(1):21–35

Amiri-Simkooei AR, Teunissen PJG, Tiberius CCJM (2009) Application of least-squares variance component estimation to GPS observables. Journal of Surveying Engineering 135(4):149–160

Babu R, Mula P, Ratnakara SC, et al (2015) IRNSS Satellite Parameter Estimation using Combination Strategy. Global Journal of Science Frontier Research 15(3)

de Bakker PF, Tiberius CCJM, van der Marel H, van Bree RJP (2012) Short and zero baseline analysis of GPS L1 C/A, L5Q, GIOVE E1B, and E5aQ signals. GPS solutions 16(1):53–64

Bensky A (2016) Wireless positioning technologies and applications. Artech House

Chandrasekhar MV, Rajarajan D, Satyanarayana G, Tirmal N, Rathnakara SC, Ganeshan AS (2015) Modernized IRNSS Broadcast Ephemeris Parameters. Control Theory and Informatics 5(2):1–9

Euler HJ, Goad CC (1991) On optimal filtering of GPS dual frequency observations without using orbit information. Bulletin Geodesique 65(2):130–143

Ganeshan AS, Ratnakara SC, Srinivasan N, Rajaram B, Tirmal N, K A (2015) First Position Fix with IRNSS. Available from: http://www.insidegnss.com/node/4545, accessed 19 April 2016. Inside GNSS pp 48–52

Godha S, Cannon M (2007) GPS/MEMS INS integrated system for navigation in urban areas. GPS Solutions 11(3):193–203

GPS Directorate (2011) Navstar GPS Space Segment/User Segment L5 interfaces (IS-GPS-705B). Technical report.

GPS World (2016) First GPS III satellite completes critical test. Available from:http://gpsworld.com/first-gps-iii-satellite-completes-critical-test/, published 19 January 2016, accessed 9 August 2016

Hofmann-Wellenhof B, Lichtenegger H, Collins J (2013) Global positioning system: theory and practice. Springer Science & Business Media

ISRO (2014a) INDIAN REGIONAL NAVIGATION SATELLITE SYSTEM: signal in space ICD for standard positioning service, Version 1.0. ISRO Satellite Centre, June 2014

ISRO (2014b) PSLV-C22/IRNSS-1A. Available from: http://www.isro.gov.in/sites/default/files/pdf/pslv-brochures/PSLVC22.pdf , accessed 1 September 2015.

ISRO (2014c) PSLV-C24/IRNSS-1B. Available from: http://www.isro.gov.in/sites/default/files/pslv-c24-brochure.pdf , published March 2014, accessed 1 September 2015

ISRO (2014d) PSLV-C26/IRNSS-1C. Available from: http://www.isro.gov.in/sites/default/files/pdf/pslv-brochures/PSLV-C26, published September 2014, accessed 1 September 2015

ISRO (2015) PSLV-C27/IRNSS-1D. Available from: http://www.isro.gov.in/sites/default/files/pdf/pslv-brochures/PSLV-C27-IRNSS-1D-BROCHURE.pdf , published March 2015, accessed 1 September 2015

ISRO (2016a) PSLV-C31/IRNSS-1E. Available from: http://www.isro.gov.in/sites/default/files/pslv-c31brochure.pdf , published January 2016, accessed 19 April 2016

ISRO (2016b) PSLV-C32/IRNSS-1F. Available from: http://www.isro.gov.in/sites/default/files/pslv-c32-final.pdf , published March 2016, accessed 19 April 2016

ISRO (2016c) PSLV-C33/IRNSS-1G. Available from: http://www.isro.gov.in/sites/default/files/pslv-c33-brochure.pdf , published April 2016, accessed 1 June 2016

Kumari A, Samal K, Rajarajan D, Swami U, Babu R, Kartik A, Rathnakara SC, Ganeshan AS (2015) Precise Modeling of Solar Radiation Pressure for IRNSS Satellite. Journal of Natural Sciences Research 5(3):35–43

Lockheed Martin (2013) Lockheed Martin Powers on the First GPS III Satellite. Available from: http://www.lockheedmartin.com.au/us/news/press-releases/2013/february/Feb28.html, published 28 February 2013, accessed 9 August 2016

Marquis W, Shaw M (2016) GPS III: Bringing new capabilities to the global community. Available from: http://www.insidegnss.com/auto/sepoct11-Marquis.pdf, accessed 9 August 2016. Inside GNSS pp 34–48

Montenbruck O, Steigenberger SR (2015) IRNSS orbit determination and broadcast ephemeris assessment. In: Proceedings of the 2015 International Technical Meeting of The Institute of Navigation, Dana Point, California, January 2015, pp 185–193

Mozo Garcia A, Piriz R, Lainez Samper MD, Romay Merino MM (2010) Multisystem Real Time Precise-Point-Positioning, today with GPS+GLONASS in the near future also with QZSS, Galileo, Compass, IRNSS. In: International Symposium on GPS/GNSS, Taipei, Tai-

wan, October 2010

Nadarajah N, Khodabandeh A, Teunissen PJG (2015) Assessing the IRNSS L5-signal in combination with GPS, Galileo, and QZSS L5/E5a-signals for positioning and navigation. doi:10.1007/s10291-015-0450-8. GPS Solutions pp 1–9

Odijk D, Teunissen PJ (2013) Characterization of between-receiver gps-galileo inter-system biases and their effect on mixed ambiguity resolution. GPS solutions 17(4):521–533

Odijk D, Teunissen PJG (2008) ADOP in closed form for a hierarchy of multi-frequency single-baseline GNSS models. Journal of Geodesy 82(8):473–492

Odijk D, Teunissen PJG, Huisman L (2012) First results of mixed GPS+GIOVE single-frequency RTK in Australia. Journal of Spatial Science 57(1):3–18

Odijk D, Nadarajah N, Zaminpardaz S, Teunissen PJG (2016) GPS, Galileo, BDS, QZSS and IRNSS Differential ISBs: Estimation and Application. GPS Solutions DOI 10.1007/s10291-016-0536-y

Odolinski R, Teunissen PJG (2016) Single-frequency, dual-GNSS versus dual-frequency, single-GNSS: a low-cost and high-grade receivers GPS-BDS RTK analysis. Journal of Geodesy pp 1–24, DOI 10.1007/s00190-016-0921-x

Rao VG (2013) Proposed LOS fast TTFF signal design for IRNSS. PhD thesis. University of Calgary

Rethika T, Mishra S, Nirmala S, Rathnakara SC, Ganeshan AS (2013) Single frequency ionospheric error correction using coefficients generated from regional ionospheric data for IRNSS. Indian Journal of radio & Space Physics 42:125–130

Sarma AD, Sultana Q, Srinivas VS (2010) Augmentation of indian regional navigation satellite system to improve dilution of precision. Journal of Navigation 63(02):313–321

Sekar SB, Sengupta S, Bandyopadhyay K (2012) Spectral compatibility of BOC (5, 2) modulation with existing GNSS signals. In: Position Location and Navigation Symposium (PLANS), 2012 IEEE/ION, IEEE, pp 886–890

Tegedor J, Øvstedal O (2014) Triple carrier precise point positioning (ppp) using gps l5. Survey Review 46(337):288–297

Teunissen PJG (1990) GPS op afstand bekeken In: een halve eeuw in de goede richting . Lustrumboek Snellius 1985-1990, DUM Delft pp 215–233

Teunissen PJG (1997) A canonical theory for short GPS baselines. Part I: The baseline precision. Journal of Geodesy 71(6):320–336

Teunissen PJG (1998a) A proof of Nielsen's conjecture on the relationship between dilution of precision for point positioning and for relative positioning with GPS. IEEE on Aerospace and Electronic Systems 34(2):693–695

Teunissen PJG (1998b) Success probability of integer gps ambiguity rounding and bootstrapping. Journal of Geodesy 72(10):606–612

Teunissen PJG (1999) An optimality property of the integer least-squares estimator. Journal of Geodesy 73(11):587–593

Teunissen PJG, Amiri-Simkooei AR (2008) Least-squares variance component estimation. Journal of Geodesy 82(2):65–82

Teunissen PJG, Odolinski R, Odijk D (2014) Instantaneous beidou+ gps rtk positioning with high cut-off elevation angles. Journal of geodesy 88(4):335–350

Thoelert S, Montenbruck O, Meurer M (2014) IRNSS-1A: signal and clock characterization of the Indian regional navigation system. GPS solutions 18(1):147–152

Verhagen S, Teunissen PJG (2014) Ambiguity resolution performance with GPS and BeiDou for LEO formation flying. Advances in Space Research 54(5):830–839

Zaminpardaz S, Teunissen PJG, Nadarajah N (2016a) GLONASS CDMA L3 ambiguity resolution and positioning. GPS solutions DOI 10.1007/s10291-016-0544-y

Zaminpardaz S, Teunissen PJG, Nadarajah N (2016b) IRNSS stand-alone positioning: first results in Australia. Journal of Spatial Science 61(1):5–27, DOI 10.1080/14498596.2016.1142398

Zhu J, Santerre R (2002) Improvement of GPS phase ambiguity resolution using prior height information as a quasi-observation. Geomatica 56(3):211–221